SCIENTIFIC REP◎RTS

OPEN

Thermal Expansion in Layered Na$_x$MO$_2$

Wataru Kobayashi[1,2,3], **Ayumu Yanagita**[1], **Takahiro Akaba**[1], **Takahiro Shimono**[1], **Daiki Tanabe**[1] **& Yutaka Moritomo** [1,2,3]

Layered oxide Na$_x$MO$_2$ (M: transition metal) is a promising cathode material for sodium-ion secondary battery. Crystal structure of O3- and P2-type Na$_x$MO$_2$ with various M against temperature (T) was systematically investigated by synchrotron x-ray diffraction mainly focusing on the T-dependences of a- and c-axis lattice constants (a and c) and z coordinate (z) of oxygen. Using a hard-sphere model with minimum Madelung energy, we confirmed that c/a and z values in O3-type Na$_x$MO$_2$ were reproduced. We further evaluated the thermal expansion coefficients (α_a and α_c) along a- and c-axis at 300 K. The anisotropy of the thermal expansion was quantitatively reproduced without adjustable parameters for O3-type Na$_x$MO$_2$. Deviations of z from the model for P2-type Na$_x$MO$_2$ are ascribed to Na vacancies characteristic to the structure.

Sodium-ion-secondary battery (SIB) stores electrochemical energy through Na$^+$ intercalation/deintercalation process. Due to large Clark number (=2.63) of Na compared with that (=0.006) of Li, SIBs can be a promising next-generation battery for storage of natural energy at a power plant and for a large-scale device such as electrical vehicle. Layered oxide Na$_x$MO$_2$ (M: transition metal) is a typical cathode material for SIBs[1–3]. Crystal structure of this material is categorized into two typical structures: O3 and P2 types[4]. Figure 1 shows schematic structures of (a) O3-type and (b) P2-type NaMO$_2$. Red, yellow, and blue spheres represent O, Na, and M, respectively. M is surrounded by six oxygens, and a MO$_6$ octahedron is formed. The edge-sharing MO$_6$ octahedra form a MO$_2$ layer. Both O3- and P2-type NaMO$_2$ exhibit alternately stacked MO$_2$ layers and Na sheets. The sodium sheet, upper and lower oxygen sheets stack as BAC resulting in the octahedral Na site. In the P2-type NaMO$_2$, the sodium and oxygen sheets stack as BAB resulting in the prismatic Na site. O3-type NaMO$_2$ (M = Ti, Cr, Mn, Co, Ni) and P2-type Na$_x$MO$_2$ (M = Mn and Co) were found to exhibit Na$^+$ intercalation/deintercalation in early 1980s[5–9]. Concerning the discovery of hard carbon (≥200 mAh/g) as anode material of SIB[10], electrochemical properties of Na$_x$MO$_2$ are extensively reported[11–20]. Very recently, substitution effects on the battery properties in O3-type structure[21–27] and P2-type structure[28–45] were extensively studied to reduce expensive element and improve the cyclability and capacity.

Not only electrochemical properties but also superconductivity[46], crystal structure[47–57], magnetism[58–61], thermoelectric effect[62,63], and first-principle calculation[64–67] of the end family are also studied. Fujita *et al.* found that Na$_x$CoO$_{2-\delta}$ single crystal shows a large dimensionless figure-of-merit of $ZT = 1$ at 800 K[63], which has motivated practical use for waste heat recovery at high temperatures (T). An isostructural O3-type LiMO$_2$ is widely used as a cathode material in lithium-ion-secondary battery (LIB)[68,69]. This family is also studied as a thermoelectric material[70] and a cathode material of solid oxide fuel cell (SOFC)[71]. In particular, Lan and Tao found that Li$_x$Al$_{0.5}$Co$_{0.5}$O$_2$ shows good proton conductivity of 0.1 Scm^{-1} at 773 K[71], which is the highest among those of known polycrystalline proton-conducting materials. During operation of energy devices such as LIB(SIB), thermoelectric device, and SOFC, these materials are exposed to a variation and/or a gradient of temperature. A mismatch in thermal expansion coefficients in between the components can result in high stresses around the interface leading to deterioration of the device. Thus, evaluation and systematical comprehension of thermal expansion behaviors in this class of materials are important.

In this paper, we report systematic structural analysis of four O3- and five P2-type Na$_x$MO$_2$ samples against T (300 K ≤ T ≤ 800 K) performed by synchrotron x-ray diffraction focusing on thermal expansion. To understand the thermal expansion behavior, we constructed a hard-sphere model with constraint that M, upper and lower oxygens are connected each other. We confirmed that the calculated d/a [d: interlayer distance, a: a-axis lattice

[1]Graduate School of Pure and Applied Sciences, University of Tsukuba, Ibaraki, 305-8571, Japan. [2]Division of Physics, Faculty of Pure and Applied Sciences, University of Tsukuba, Ibaraki, 305-8571, Japan. [3]Tsukuba Research Center for Energy Materials Science (TREMS), University of Tsukuba, Ibaraki, 305-8571, Japan. Correspondence and requests for materials should be addressed to W.K. (email: kobayashi.wataru.gf@u.tsukuba.ac.jp)

1
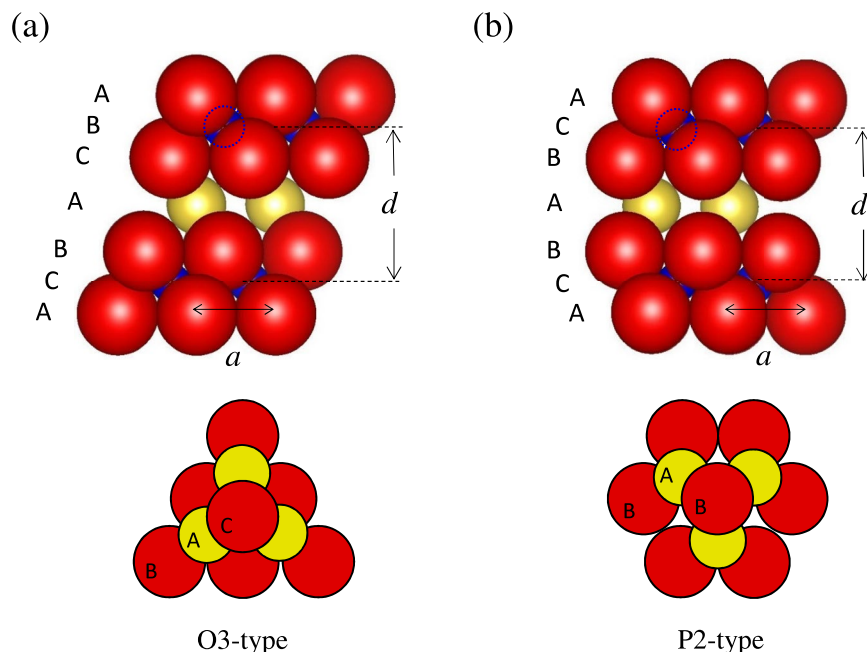
Figure 1. Schematic figure of (**a**) O3- and (**b**) P2-NaMO$_2$ structure. Red, yellow, and blue spheres represent O, Na, and M (transition metal element), respectively. M is sandwiched by upper and lower oxygen layers. In the P2-type structure, only the Na1 site [the atomic coordinates of Na1 are $\left(\frac{1}{3}, \frac{2}{3}, \frac{3}{4}\right)$] is shown. The bottom panels show top views of O-Na-O stackings in the O3- and P2-type structures, respectively. The BAC stacking in O3 forms NaO$_6$ octahedron, and the BAB stacking in P2 forms NaO$_6$ triangular prism.

constant] and z well reproduced the experimental values for O3-type Na$_x$MO$_2$. By introducing T-linear expansion of the hard sphere, the anisotropy of the thermal expansion was quantitatively reproduced without adjustable parameter for O3-type Na$_x$MO$_2$.

Results
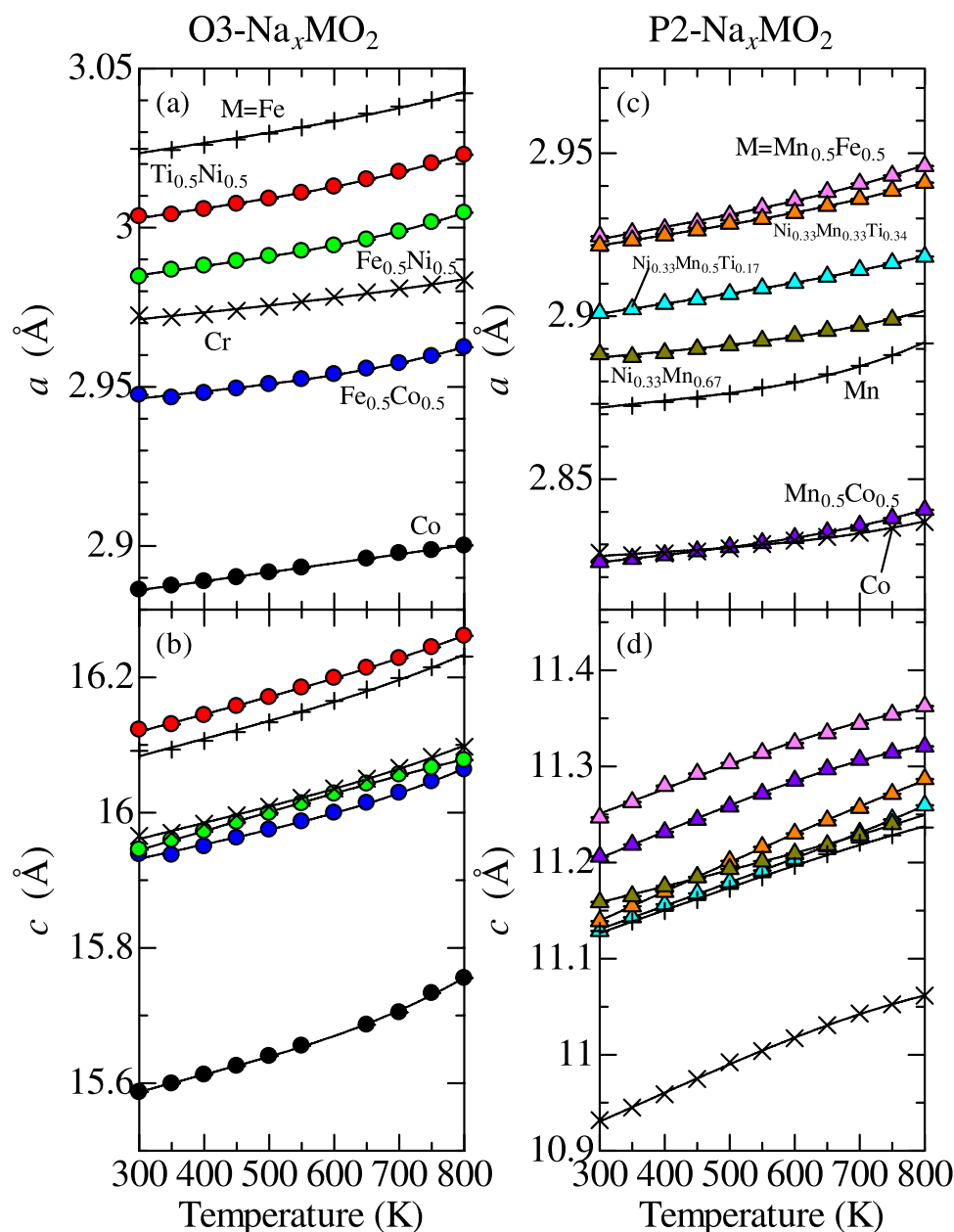
Temperature dependence of $a(c)$-axis lattice constants and z coordinate of oxygen. Figure 2(a) and (b) show a-axis lattice constant (a), and (b) c-axis lattice constant (c) of O3-type Na$_{0.99}$CrO$_2$, Na$_{0.99}$FeO$_2$, Na$_{1.00}$CoO$_2$, Na$_{0.98}$Fe$_{0.5}$Co$_{0.5}$O$_2$, Na$_{0.99}$Fe$_{0.5}$Ni$_{0.5}$O$_2$, and Na$_{0.94}$Ti$_{0.5}$Ni$_{0.5}$O$_2$ against T. With T, a and c monotonically increase. Raw x-ray diffraction data and results of Rietveld refinements at 300 K are shown in Figs S1–S3. The solid line represents a least-square fitting with use of a degree 3 polynomial function. By using $\alpha_{a(c)} = \frac{d \ln a(c)}{dT}$, a linear thermal expansion coefficient along a- and c-axis was evaluated. Figure 2(c) and (d) show a and c of P2-type Na$_{0.52}$MnO$_2$, Na$_{0.59}$CoO$_2$, Na$_{0.50}$Mn$_{0.5}$Co$_{0.5}$O$_2$, Na$_{0.70}$Ni$_{0.33}$Mn$_{0.67}$O$_2$, Na$_{0.69}$Ni$_{0.33}$Mn$_{0.5}$Ti$_{0.17}$O$_2$, Na$_{0.70}$Ni$_{0.33}$Mn$_{0.33}$Ti$_{0.34}$O$_2$, and Na$_{0.48}$Mn$_{0.5}$Fe$_{0.5}$O$_2$. The P2-type compounds also show monotonical T-dependences of a and c. In Table 1, the values of a, c at 300 K, α_a, and α_c of O3- and P2-type Na$_x$MO$_2$ at 300 K were listed.

Figure 3(a) shows z coordinate of oxygen for O3- and P2-type structure (z_{O3} and z_{P2}) against a at 300 and 700 K. Blue and red circles represent z_{O3} at 300 and 700 K, respectively. Light green and pink triangles represent z_{P2} at 300 and 700 K, respectively. The values were almost independent of T. Figure 3(b) shows a ratio of interlayer distance (d) to a against a at 300 K, where d is $c/3$ for O3-type and $c/2$ for P2-type structure. Light blue and purple circles represent d/a of O3-type compounds at 300 and 700 K, respectively. Green and yellow triangles represent d/a of P2-type compounds at 300 and 700 K, respectively. d/a slightly decreases with an increase in a.

Thermal expansion coefficients. Figure 4 shows (a) α_a, (b) α_c, and (c) α_c/α_a against a. α_a and α_c of O3-type Na$_{1.00}$CoO$_2$ were 0.98×10^{-5} K^{-1} and 1.71×10^{-5} K^{-1}, respectively. These values are comparable to those of inorganic compounds; $\alpha_a = 1.44 \times 10^{-5}$ K^{-1} for LiMn$_2$O$_4$[72], and $\alpha_a(\alpha_c) = 0.85(2.5) \times 10^{-5}$ K^{-1} for layered BaFe$_{1.84}$Co$_{0.16}$As$_2$[73]. $\alpha_a(\alpha_c)$ in Fig. 4 is rather scattered against a around the averaged value of $0.92(1.96) \times 10^{-5}$ K^{-1}. The ratio α_c/α_a is also scattered around the averaged value ($=2.30$). However, the data point for P2-Na$_{0.59}$CoO$_2$ are seriously deviated from the average value. This is probably due to the Na ordering[67].

Discussion

A hard-sphere model with minimum Madelung energy. We have constructed a hard-sphere structural model for O3- and P2-type NaMO$_2$ to reproduce the experimental results (d/a, z, α_c/α_a). Firstly, imagine a sheet consists of hard spheres that were arrayed on triangular lattice, and then the sheet is alternately stacked as shown in Fig. 1. In the model, hard spheres of Na, M, and O were assumed to have Shannon's ionic radius[74]; $R_{Na} = 1.02$ Å, $R_O = 1.40$ Å, and R_M is a variable parameter that takes 0.58–0.7 Å, respectively. Since the ionic radius of the hard sphere is different from one another, the structure can not be the hexagonal close-packed structure, and several

Figure 2. Temperature (T) dependence of (**a**) a-axis, (**b**) c-axis lattice constants (a and c) of O3-type Na_xMO_2. T dependence of (**c**) a, and (**d**) c of P2-type Na_xMO_2. The solid line represents a least-square fitting with use of a degree 3 polynomial function for a and c. a and c values of O3-$Na_{0.99}CrO_2$, O3-$Na_{0.99}FeO_2$, P2-$Na_{0.52}MnO_2$, and P2-$Na_{0.59}CoO_2$ were referred from our previous reports[56,57].

structures with different a are possible for the unique value of R_M. Here, we adopted a constraint that M, upper, and lower oxygens coroneted each other, because the constraint minimizes the Madelung energy against a (vide infra). For a calculation of thermal expansion coefficient, the hard sphere is assumed to expand in proportion to the temperature difference (ΔT). ΔT dependence of R_{Na} is expressed as $R_{Na}(\Delta T) = R_{Na} + Am_{Na}^{-1}R_{Na}\Delta T$, where $m_{Na}(=22.99)$ is atomic weight of Na atom. Similarly, ΔT dependences of R_O and R_M are expressed as $R_O(\Delta T) = R_O + Am_O^{-1}R_O\Delta T$, and $R_M(\Delta T) = R_M + Am_M^{-1}R_M\Delta T$, where $m_O(=16.00)$ and $m_M(=55.85)$ (We used 55.85 of the atomic weight of Fe as m_M although M is not only Fe but also mixture of Ti, Mn, Fe, and Co. When we used 47.88 of the atomic weight of Ti as m_M, the calculated α_c/α_a worse reproduces the experiments.) are atomic weights of O and M, respectively.

Now, let us derive the expression (a^{calc}) of a-axis lattice constant as a function of ΔT. Note that the in-plane nearest-neighbor oxygen distance is a for both the P2- and O3-structure. Considering the above-mentioned constraint, $a^{calc}(\Delta T)$ for both O3- and P2-structures is expressed as

| Compound	a (Å)	c (Å)	z	α_a (10^{-5} K^{-1})	α_c (10^{-5} K^{-1})	α_c/α_a
[56]O3-Na$_{0.99}$CrO$_2$	†2.97247(3)	†15.96540(18)	0.23213(13)	*0.73	*1.52	*2.07
[56]O3-Na$_{0.99}$FeO$_2$	†3.02477(2)	†16.09135(10)	0.23389(12)	*1.07	*1.63	*1.52
O3-Na$_{1.00}$CoO$_2$	2.88627(2)	15.58680(12)	0.23046(9)	0.98	1.71	1.74
O3-Na$_{0.98}$Fe$_{0.5}$Co$_{0.5}$O$_2$	2.94748(3)	15.93844(23)	0.23238(12)	0.79	1.37	1.73
O3-Na$_{0.99}$Fe$_{0.5}$Ni$_{0.5}$O$_2$	2.98463(9)	15.94545(63)	0.23334(17)	1.01	1.76	1.74
O3-Na$_{0.94}$Ti$_{0.5}$Ni$_{0.5}$O$_2$	3.00358(4)	16.12273(24)	0.23382(13)	1.06	1.61	1.51
[57]P2-Na$_{0.52}$MnO$_2$	†2.87311(9)	†11.1287(5)	0.0858(3)	*0.81	*2.11	*2.59
[57]P2-Na$_{0.59}$CoO$_2$	†2.82748(4)	†10.9319(2)	0.0881(3)	*0.48	*2.70	*5.61
P2-Na$_{0.50}$Mn$_{0.5}$Co$_{0.5}$O$_2$	2.82459(5)	11.20617(33)	0.08704(24)	0.84	2.42	2.87
P2-Na$_{0.70}$Ni$_{0.33}$Mn$_{0.67}$O$_2$	2.88835(5)	11.15881(29)	0.09120(28)	0.67	1.51	2.26
P2-Na$_{0.69}$Ni$_{0.33}$Mn$_{0.5}$Ti$_{0.17}$O$_2$	2.90101(3)	11.12868(16)	0.09263(17)	1.07	2.20	2.05
P2-Na$_{0.70}$Ni$_{0.33}$Mn$_{0.33}$Ti$_{0.34}$O$_2$	2.92173(4)	11.13896(22)	0.09381(21)	1.12	2.72	2.42
P2-Na$_{0.48}$Mn$_{0.5}$Fe$_{0.5}$O$_2$	2.92452(8)	11.24690(48)	0.08592(32)	1.30	2.26	1.74

Table 1. a-axis, c-axis lattice constants (a and c), z coordinate of oxygen (z) at 300 K, the linear thermal expansion coefficient [α_a (α_c)] along a(c)-axis, and α_c/α_a of O3- and P2-type Na$_x$MO$_2$ at 300 K. †The original data were referred from previous reports[56,57]. *α_a and α_c were reevaluated in a T-range of 300–800 K.
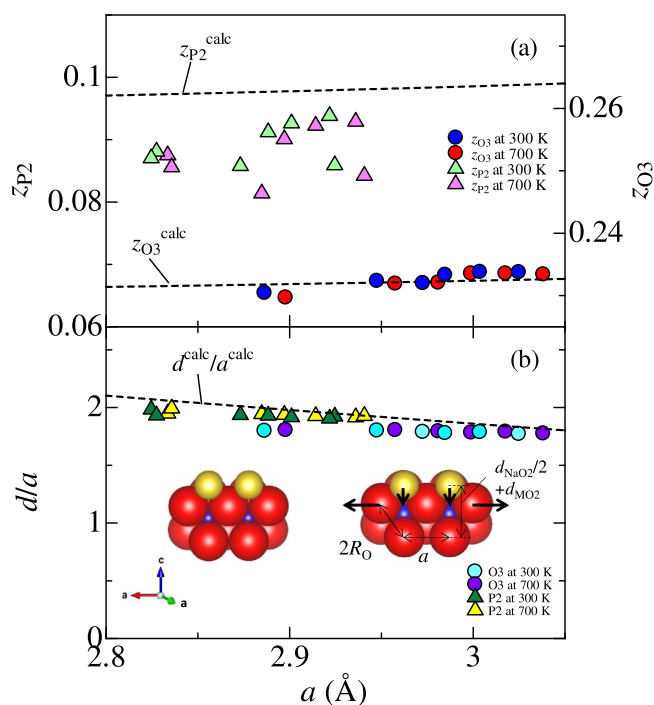
Figure 3. (**a**) z coordinate of oxygen for O3- (z_{O3}) and P2-type (z_{P2}) structure against a-axis lattice constant (a). Blue and red circles represent z_{O3} at 300 and 700 K, respectively. Light green and pink triangles represent z_{P2} at 300 and 700 K, respectively. The broken lines represent z calculated by the hard sphere model with minimum Madelung energy for O3 and P2-type compounds (z_{O3}^{calc} and z_{P2}^{calc}) against a, respectively. (**b**) The ratio of interlayer distance (d) to a against a. Light blue and purple circles represent d/a of O3-type compounds at 300 and 700 K, respectively. Green and yellow triangles represent d/a of P2-type compounds at 300 and 700 K, respectively. The broken line represents d/a calculated by the hard sphere model with minimum Madelung energy (d^{calc}/a^{calc}) against a. The inset of Fig. 3(b) shows a schematic view of the local atomic configuration around M.

$$a^{calc}(\Delta T) = 2\sqrt{[R_O(\Delta T) + R_M(\Delta T)]^2 - R_O(\Delta T)^2}. \tag{1}$$

This equation is easily derived using Pythagorean theorem. As shown in Eq. 1, a^{calc} strongly depends on R_M value. Due to the finite ionic radius of oxygen ($R_O = 1.40$ Å), minimum value of a^{calc} is 2.80 Å. At $a^{calc} = 2.80$ Å, R_M is evaluated to be ≈0.5799 Å using Eq. 1. With an increase in R_M, the oxygen triangular lattice expands in order to keep the connection between M, upper and lower oxygens.
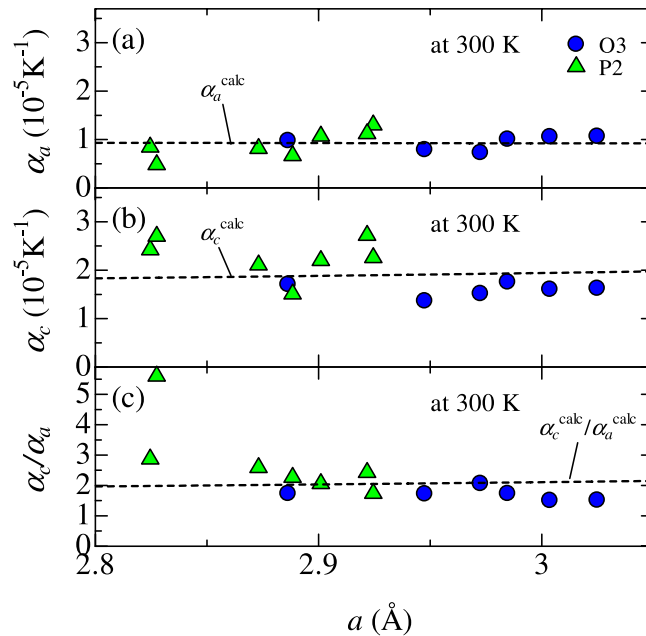
Figure 4. Linear thermal expansion coefficient (**a**) along a-axis (α_a), (**b**) along c-axis (α_c), and (**c**) α_c/α_a against a-axis lattice constant (a). The broken lines in Fig. 4(a,b and c) represent α_a, α_c, and α_c/α_a against a calculated by the hard-sphere model with minimum Madelung energy (α_a^{calc}, α_c^{calc}, and $\alpha_c^{\text{calc}}/\alpha_a^{\text{calc}}$).

Na sheet is sandwiched by the MO_2 layers as BAC (BAB) in the O3-type (P2-type) structure. We noted that the expression (d^{calc}) of interlayer distance is independent of the stacking manner, and the ΔT-dependence of d^{calc} for O3- and P2-type structure is expressed as,

$$d^{\text{calc}}(\Delta T) = \sqrt{[2R_O(\Delta T)]^2 - \frac{a^{\text{calc}}(\Delta T)^2}{3}} + 2\sqrt{[R_O(\Delta T) + R_{Na}(\Delta T)]^2 - \frac{a^{\text{calc}}(\Delta T)^2}{3}}. \tag{2}$$

The first and the second terms correspond to $d_{MO_2}^{\text{calc}}$ and $d_{NaO_2}^{\text{calc}}$, where $d_{MO_2}^{\text{calc}}$ and $d_{NaO_2}^{\text{calc}}$ are the thicknesses of MO_2 and NaO_2 layers, respectively. A relationship between d^{calc} and the expression of c (c^{calc}) is expressed as $3d^{\text{calc}}(\Delta T) = c_{O3}^{\text{calc}}(\Delta T)$ and $2d^{\text{calc}}(\Delta T) = c_{P2}^{\text{calc}}(\Delta T)$ for O3- and P2-type structures. By using Pythagorean theorem, Eq. 2 is easily derived. Expressions of z (z^{calc}) for O3- and P2-type structures are derived as

$$z_{O3}^{\text{calc}}(\Delta T) = \frac{1}{6} + \frac{1}{6d^{\text{calc}}(\Delta T)}\sqrt{[2R_O(\Delta T)]^2 - \frac{a^{\text{calc}}(\Delta T)^2}{3}}, \tag{3}$$

and

$$z_{P2}^{\text{calc}}(\Delta T) = \frac{1}{4d^{\text{calc}}(\Delta T)}\sqrt{[2R_O(\Delta T)]^2 - \frac{a^{\text{calc}}(\Delta T)^2}{3}}, \tag{4}$$

respectively.

Now, let us consider the stability of the hard-sphere model with the constraint that M, upper and lower oxygens coroneted to each other. For this purpose, we calculated the Madelung energy at a specific R_M ($=0.65$ Å) against a. We show that this model exhibits minimum Madelung energy (E_{ME}). Figure 5 shows E_{ME} of O3- and P2-type $NaMO_2$ against a. Our constraint gives $a^{\text{calc}} \approx 2.995$ Å [Eq. 1] at $R_M = 0.65$ Å. With the O3 structure, the a^{calc} value corresponds to the minimum position of E_{ME} (-8.67 eV). With an increase in a from 2.995 Å, M becomes isolated from the surrounding oxygens (the right-side inset of Fig. 5), and E_{ME} increases (Note that the oxygen positions were controlled by Eqs 3 and 4). With an decrease in a from 2.995 Å, the upper and lower oxygens are separated (the left-side inset of Fig. 5), and E_{ME} increases as well (We used $d^{\text{calc}} = 2\sqrt{(R_M + R_O)^2 - \frac{a^2}{3}} + 2\sqrt{[R_O + R_{Na}]^2 - \frac{a^2}{3}}$, $z_{O3}^{\text{calc}} = \frac{1}{6} + \frac{1}{6d^{\text{calc}}}\sqrt{(R_M + R_O)^2 - \frac{a^2}{3}}$, and $z_{P2}^{\text{calc}} = \frac{1}{4d^{\text{calc}}}\sqrt{(R_M + R_O)^2 - \frac{a^2}{3}}$ for the calculation below $a = 2.995$ Å). Similar results are obtained for the P2 structure. Thus, our model is energetically stable against the variation of a. Our constraint that M, upper and lower oxygens connected to each other causes the compact layered structure and minimized the long-range Coulomb energy between the layers. We call our model "hard-sphere model with minimum Madelung energy".
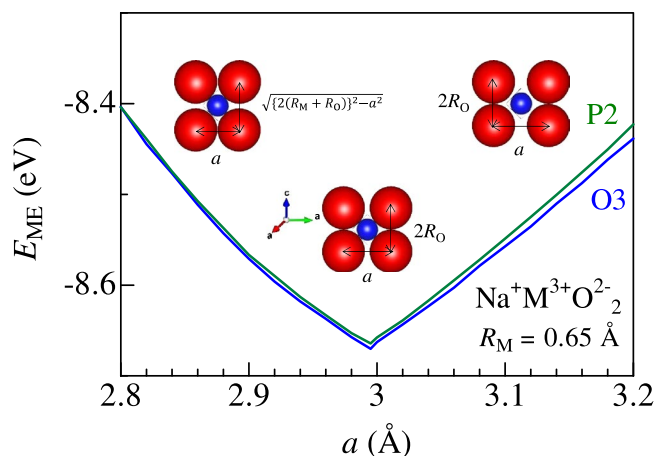
Figure 5. Madelung energy (E_{ME}) of O3- and P2-type NaMO$_2$ against a for the hard-sphere model. R_M was fixed at 0.65 Å.

Companion of the structural parameters and the thermal expansion coefficients with the model.

The broken line in Fig. 3(b) is the calculated d/a based on the hard-sphere model with minimum Madelung energy (see Eqs 1 and 2). d^{calc}/a^{calc} decreases with an increase in a^{calc}, which reproduces experimental results. The decrease in d^{calc}/a^{calc} is schematically depicted in the inset of Fig. 3(b). When O-O distance along in-plane direction elongates due to increase in R_M, Na atoms relatively sink down along out-of-plane direction. (Decrease in $d_{NaO_2}/(2a)$ against a is displayed in Fig. S5). We further calculated z and plotted them in Fig. 3(a). In the O3-type compounds, z^{calc} well reproduces the experimental data. In the P2-type compounds, however, z^{calc} is slightly smaller than z_{P2}^{calc}. We ascribed the smaller z_{P2} to the Na vacancies characteristic to the P2 structure. With the vacancies, the nominal valence of M became higher, and hence R_M becomes smaller. Our model tells us that z_{P2}^{calc} becomes smaller if R_M becomes smaller.

The broken lines in Fig. 4 represent the calculated α_a, α_c, and α_c/α_a (α_a^{calc}, α_c^{calc}, and $\alpha_c^{calc}/\alpha_a^{calc}$), respectively. $\alpha_a^{calc}(\alpha_c^{calc})$ was evaluated by using the equation, $\frac{d \ln a^{calc}(\Delta T)}{d\Delta T}\left[\frac{d \ln c^{calc}(\Delta T)}{d\Delta T}\right]$. The only fitting parameter A ($=2.56 \times 10^{-4}$ K^{-1}) was chosen to fit the average value of α_a ($=0.92 \times 10^{-5}$ K^{-1}). Using the same value of A, α_c^{calc} was found to reproduce the magnitude of experimental value for the O3 materials. On the other hand, larger α_c^{calc} for the P2 materials is possibly due to Na vacancies except for the data point of Na$_{0.59}$CoO$_2$. We note that $\frac{\alpha_c^{calc}}{\alpha_a^{calc}}$ is expressed without the adjustable parameter A,

$$
\left.\frac{\alpha_c^{calc}}{\alpha_a^{calc}}\right|_{\Delta T=0} = \frac{\frac{2m_O^{-1}R_O^2}{m_M^{-1}R_M R_O + (m_O^{-1}R_O + m_M^{-1}R_M)R_M} - \frac{2}{3}}{4\sqrt{\left\{\left(\frac{2R_O}{a_0}\right)^2 - \frac{1}{3}\right\}\left\{\left(\frac{R_O + R_{Na}}{a_0}\right)^2 - \frac{1}{3}\right\} + 2\left\{\left(\frac{2R_O}{a_0}\right)^2 - \frac{1}{3}\right\}}}
$$
$$
+ \frac{\frac{(m_O^{-1}R_O + m_{Na}^{-1}R_{Na})(R_O + R_{Na})}{2m_M^{-1}R_M R_O + 2(m_O^{-1}R_O + m_M^{-1}R_M)R_M} - \frac{2}{3}}{\sqrt{\left\{\left(\frac{2R_O}{a_0}\right)^2 - \frac{1}{3}\right\}\left\{\left(\frac{R_O + R_{Na}}{a_0}\right)^2 - \frac{1}{3}\right\} + 2\left\{\left(\frac{R_O + R_{Na}}{a_0}\right)^2 - \frac{1}{3}\right\}}},
$$

(5)

where $a_0 = 2\sqrt{2R_O R_M + R_O^2}$. The hard-sphere model examined in this paper gives intuitive and easy comprehension of the thermal expansion behavior of the layered oxides. The density-functional-thery (DFT) calculation successfully reproduces the linear thermal expansion coefficients of several materials such as Al[75], S[76], 4d transition metals[77,78], Os[78], MgO[79], CaO[79], and ZnO[80], which is beyond the scope of this paper.

Conclusion

We systematically determined the temperature dependent lattice constant and z-coordinates of P2- and O3-type NaMO$_2$. We proposed a simple hard-sphere model with constraint that M, upper and lower oxygens are coroneted to each others. The model quantitatively reproduced a, c, z, α_a and α_c for O3-type Na$_x$MO$_2$. On the other hand, z coordinate of P2-type Na$_x$MO$_2$ deviates from the hard-sphere model possibly due to Na vacancies. This simple model can be easily applied for the other layered compounds to intuitively understand and design the thermal expansion behaviors.

Methods

Sample preparation. Powders of O3- and P2-Na$_x$MO$_2$ (M: transition metal) were synthesized by using conventional solid state reaction. For O3-Na$_{1.00}$CoO$_2$, Na$_2$O$_2$ and Co$_3$O$_4$ were mixed under the molar ratio of Na:Co = 1.1:1, and calcined at 550°C in O$_2$ for 16 h. Then, the product was finely ground, and again calcined in the same condition (this process was repeated once again.). For O3-Na$_{0.98}$Fe$_{0.5}$Co$_{0.5}$O$_2$, Na$_2$CO$_3$, Fe$_3$O$_4$ and Co$_3$O$_4$ were mixed under the molar ratio of Na:Fe:Co = 1.05:0.5:0.5, and calcined at 900°C in air for 15 h. For

$O3\text{-}Na_{0.99}Fe_{0.5}Ni_{0.5}O_2$, Na_2O_2, Fe_2O_3 and NiO were mixed under the molar ratio of Na:Fe:Ni = 1.2:0.5:0.5, and calcined at 650°C in O_2 for 15 h. Then the product was finely ground and again calcined in the same condition. For $O3\text{-}Na_{0.94}Ti_{0.5}Ni_{0.5}O_2$, Na_2CO_3, TiO_2 and NiO were mixed under the molar ratio of Na:Ti:Ni = 1.05:0.5:0.5, and calcined at 900°C in air for 15 h. Then the product was finely ground and again calcined in the same condition. For $P2\text{-}Na_{0.50}Mn_{0.5}Co_{0.5}O_2$, Na_2CO_3, $MnCO_3$ and Co_3O_4 were mixed under the molar ratio of Na:Mn:Co = 0.7:0.5:0.5, and calcined at 900°C in air for 12 h, Then, the product was finely ground and again calcined in the same condition. For $P2\text{-}Na_{0.70}Ni_{0.33}Mn_{0.67}O_2$, Na_2CO_3, NiO and Mn_2O_3 were mixed in ethanol under the molar ratio of Na:Ni:Mn = 0.7:0.33:0.67, and calcined at 900°C in air for 24 h. Then, the product was finely ground and again calcined in the same condition. For $P2\text{-}Na_{0.69}Ni_{0.33}Mn_{0.5}Ti_{0.17}O_2$, Na_2CO_3, NiO, Mn_2O_3 and TiO_2 were mixed under the molar ratio of Na:Ni:Mn:Ti = 0.7:0.33:0.5: 0.17, and calcined at 900°C in air for 18 h. For $P2\text{-}Na_{0.70}Ni_{0.33}Mn_{0.33}Ti_{0.34}O_2$, Na_2CO_3, NiO, Mn_2O_3 and TiO_2 were mixed under the molar ratio of Na:Ni:Mn:Ti = 0.7:0.33:0.33:0.34, and calcined at 900°C in air for 12 h. For $P2\text{-}Na_{0.48}Mn_{0.5}Fe_{0.5}O_2$, Na_2O_2, Mn_2O_3 and Fe_2O_3 were mixed under the molar ratio of Na:Mn:Fe = 0.7:0.5:0.5, and calcined at 900°C in air for 12 h. Then, the product was finely ground and again calcined in the same condition. All the samples were taken out from the hot furnace (>200°C), and then immediately transferred into a vacuum desiccator to avoid moisture in air.

X-ray diffraction.

The synchrotron radiation x-ray diffraction (XRD) patterns were measured at BL02B2 beamline[81] at SPring-8. The capillary was placed on the Debye-Scherrer camera at the beamline. The sample temperature was controlled by blowing a hot N_2 in the temperature range of $300\,K \leq T \leq 800\,K$. The XRD patterns were detected with an imaging plate (IP). The exposure time was 5 min. The wavelength of the x-ray was 0.499420 Å for $P2\text{-}Na_{0.48}Mn_{0.5}Fe_{0.5}O_2$ and $P2\text{-}Na_{0.50}Mn_{0.5}Co_{0.5}O_2$, and 0.499892 Å for $O3\text{-}Na_{0.98}Fe_{0.5}Co_{0.5}O_2$ and $Na_{0.94}Ti_{0.5}Ni_{0.5}O_2$, and 0.499838 Å for the others. The wavelengths are calibrated by the cell parameter of standard CeO_2 powders. Crystal structure was analyzed by RIETAN-FP program[82]. Schematic figure of the crystal structure were drawn by VESTA program[83]. All the reflections can be indexed with the O3-type ($R\bar{3}m$) or P2-type ($P6_3/mmc$) structures except for a tiny amount of impurity of O3-type Fe-rich phase for $Na_{0.99}Fe_{0.5}Ni_{0.5}O_2$ and NiO for $Na_{0.94}Ti_{0.5}Ni_{0.5}O_2$. All the structural parameters against T ($300\,K \leq T \leq 800\,K$) were listed in Tables S1–S9. During heating process, any extra impurity peaks were not appeared. We observed no tendency of Na deintercalation due to heating (Fig. S4).

The actual Na concentrations in the compound were determined by the Rietveld refinement based on the synchrotron XRD patterns at 300 K. We note that ref.[45] reported a consistency of Na contents determined by ICP-AES (Inductively Coupled Plasma Atomic Emission Spectroscopy) and Rietveld refinement using synchrotron x-ray diffraction for $P2\text{-}Na_xMn_{1/2}Fe_{1/2}O_2$ phase.

Madelung energy calculation.

Madelung energy (E_{ME}) was computed by the MADEL program in the VESTA software using the Fourier method[83]. The site potential ϕ_i is calculated by the formula $\phi_i = \sum_j \frac{g_j Z_j}{4\pi\varepsilon_0 l_{ij}}$, where g_j is the occupancy of the j th ion, Z_i is the valence of the j th ion, ε_0 is the vacuum permittivity, and l_{ij} is the distance between ions i and j. E_{ME} is calculated by using the formula $E_{ME} = \frac{1}{2}\sum_i \phi_i Z_i W_i$, where W_i is a factor depending on g_i and the number of equivalent atomic positions at the site i in the unit cell. For O3-type structure (space group: $R\bar{3}m$), we put +1, +3, and −2 charges on 3a Na (0,0,0), 3b M (0,0,$\frac{1}{2}$), and 6c O (0,0,z) sites in stoichiometric $NaMO_2$. In the calculation of the P2-type structure ($P6_3/mmc$), we assume a stoichiometric $NaMO_2$ with fully occupied 2d Na site. We put $+e$, $+3e$, and $−2e$ charges on 2d Na $\left(\frac{1}{3}, \frac{2}{3}, \frac{3}{4}\right)$, 2a M (0,0,0), and 4f O $\left(\frac{1}{3}, \frac{2}{3}, z\right)$. A radius ($s$) of the hard sphere was set to 0.3 Å, and Fourier coefficients are summed up to 10 Å^{-1} in the reciprocal space.

References

1. Kim, S. W., Seo, D. H., Ma, X., Ceder, G. & Kang, K. Electrode materials for rechargeable sodium-ion batteries: Potential alternatives to current lithium-ion batteries. *Advanced Energy Materials* **2**, 710–721 (2012).
2. Pan, H., Hu, Y.-S. & Chen, L. Room-temperature stationary sodium-ion batteries for large-scale electric energy storage. *Energy Environ. Sci.* **6**, 2338–2360 (2013).
3. Yabuuchi, N., Kubota, K., Dahbi, M. & Komaba, S. Research Development on Sodium-Ion Batteries. *Chem. Rev.* **114**, 11636–11682 (2014).
4. Delmas, C., Fouassier, C. & Hagenmuller, P. Structural classification and properties of the layered oxides. *Physica* **99B**, 81–85 (1980).
5. Parant, J. P., Olazcuaga, R., Devalette, M., Fouassier, C. & Hagenmuller, P. Sur quelques nouvelles phases de formule Na_xMnO_2 ($x \leq 1$). *J. Solid State Chem.* **3**, 1–11 (1971).
6. Delmas, C., Braconnier, J. J., Fouassier, C. & Hagenmuller, P. Electrochemical intercalation of sodium in Na_xCoO_2 bronzes. *Solid State Ionics* **3/4**, 165–169 (1981).
7. Braconnier, J. J., Delmas, C. & Hagenmuller, P. Etude par Desintercalation Electrochimique des Systemes Na_xCrO_2 et Na_xNiO_2. *Mat. Res. Bull.* **17**, 993–1000 (1982).
8. Maazaz, A., Delmas, C. & Hagenmuller, P. A study of the Na_xTiO_2 system by electrochemical deintercalation. *J. Incl. Phenom.* **1**, 45–51 (1983).
9. Mendiboure, A., Delmas, C. & Hagenmuller, P. Electrochemical Intercalation and Deintercalation of Na_xMnO_2 Bronzes. *J. Solid State Chem.* **57**, 323–331 (1985).
10. Komaba, S. *et al.* Electrochemical Na Insertion and Solid Electrolyte Interphase for Hard-Carbon Electrodes and Application to Na-Ion Batteries. *Adv. Energy Mater.* **21**, 3859–3867 (2011).
11. Komaba, S., Takei, C., Nakayama, T., Ogata, A. & Yabuuchi, N. Electrochemical intercalation activity of layered $NaCrO_2$ vs. $LiCrO_2$. *Electrochem. commun.* **12**, 355–358 (2010).
12. Didier, C. *et al.* Electrochemical Na-Deintercalation from $NaVO_2$. *Electrochem. Solid-State Lett.* **14**, A75–A78 (2011).
13. Ma, X., Chen, H. & Ceder, G. Electrochemical Properties of Monoclinic $NaMnO_2$. *J. Electrochem. Soc.* **158**, 1307–1312 (2011).
14. Nohira, T., Ishibashi, T. & Hagiwara, R. Properties of an intermediate temperature ionic liquid NaTFSA-CsTFSA and charge-discharge properties of $NaCrO_2$ positive electrode at 423 K for a sodium secondary battery. *J. Power Sources* **205**, 506–509 (2012).

15. Lee, E. *et al*. New Insights into the Performance Degradation of Fe-Based Layered Oxides in Sodium-Ion Batteries: Instability of Fe^{3+}/Fe^{4+} Redox in α-NaFeO$_2$. *Chem. Mater.* **27**, 6755–6764 (2015).

16. Wu, D. *et al*. NaTiO$_2$: a layered anode material for sodium-ion batteries. *Energy Environ. Sci.* **8**, 195–202 (2015).

17. Caballero, A. *et al*. Synthesis and characterization of high-temperature hexagonal P2-Na$_{0.6}$MnO$_2$ and its electrochemical behaviour as cathode in sodium cells. *J. Mater. Chem.* **12**, 1142–1147 (2002).

18. Hamani, D., Ati, M., Tarascon, J. M. & Rozier, P. P2-Na$_x$VO$_2$ as possible electrode for Na-ion batteries. *Electrochem. Commun.* **13**, 938–941 (2011).

19. D'Arienzo, M. *et al*. Layered Na$_{0.71}$CoO$_2$: a powerful candidate for viable and high performance Na-batteries. *Phys. Chem. Chem. Phys.* **14**, 5945–5952 (2012).

20. Zhu, K. *et al*. A New Layered Sodium Molybdenum Oxide Anode for Full Intercalation-Type Sodium-Ion Batteries. *J. Mater. Chem. A* **3**, 22012–22016 (2015).

21. Saadoune, I., Maazaz, A., Mé Né Trier, M. & Delmas, C. On the Na$_x$Ni$_{0.6}$Co$_{0.4}$O$_2$ System: Physical and Electrochemical Studies. *J. Solid State Chem.* **122**, 111–117 (1996).

22. Yoshida, H., Yabuuchi, N. & Komaba, S. NaFe$_{0.5}$Co$_{0.5}$O$_2$ as high energy and power positive electrode for Na-ion batteries. *Electrochem. Commun.* **34**, 60–63 (2013).

23. Mu, L. *et al*. Prototype Sodium-Ion Batteries Using an Air-Stable and Co/Ni-Free O3-Layered Metal Oxide Cathode. *Adv. Mater.* **27**, 6928–6933 (2015).

24. Singh, G. *et al*. Electrochemical performance of NaFe$_x$(Ni$_{0.5}$Ti$_{0.5}$)$_{1-x}$O$_2$ ($x = 0.2$ and $x = 0.4$) cathode for sodium-ion battery. *J. Power Sources* **273**, 333–339 (2015).

25. Vassilaras, P., Toumar, A. J. & Ceder, G. Electrochemical properties of NaNi$_{1/3}$Co$_{1/3}$Fe$_{1/3}$O$_2$ as a cathode material for Na-ion batteries. *Electrochem. Commun.* **38**, 79–81 (2014).

26. Wang, X., Liu, G., Iwao, T., Okubo, M. & Yamada, A. Role of Ligand-to-Metal Charge Transfer in O3-Type NaFeO$_2$-NaNiO$_2$ Solid Solution for Enhanced Electrochemical Properties. *J. Phys. Chem. C* **118**, 2970–2976 (2014).

27. Yu, H., Guo, S., Zhu, Y., Ishida, M. & Zhou, H. Novel titanium-based O3-type NaTi$_{0.5}$Ni$_{0.5}$O$_2$ as a cathode material for sodium ion batteries. *Chem. Commun.* **50**, 457–459 (2014).

28. Yabuuchi, N. *et al*. P2-type Na$_x$[Fe$_{1/2}$Mn$_{1/2}$]O$_2$ made from earth-abundant elements for rechargeable Na batteries. *Nat. Mater.* **11**, 512–517 (2012).

29. Buchholz, D., Chagas, L. G., Winter, M. & Passerini, S. P2-type layered Na$_{0.45}$Ni$_{0.22}$Co$_{0.11}$Mn$_{0.66}$O$_2$ as intercalation host material for lithium and sodium batteries. *Electrochimica Acta.* **110**, 208–213 (2013).

30. Doubaji, S., Valvo, M., Saadoune, I., Dahbi, M. & Edström, K. Synthesis and characterization of a new layered cathode material for sodium ion batteries. *J. Power Sources* **266**, 275–281 (2014).

31. Yoshida, H. *et al*. P2-type Na$_{2/3}$Ni$_{1/3}$Mn$_{2/3-x}$Ti$_x$O$_2$ as a new positive electrode for higher energy Na-ion batteries. *Chem. Commun.* **50**, 3677–3680 (2014).

32. Chen, X. *et al*. Stable layered P3/P2 Na$_{0.66}$Co$_{0.5}$Mn$_{0.5}$O$_2$ cathode materials for sodium-ion batteries. *J. Mater. Chem. A* **3**, 20708–20714 (2015).

33. Kang, W. *et al*. Copper substituted P2-type Na$_{0.67}$Cu$_x$Mn$_{1-x}$O$_2$: a stable high-power sodium-ion battery cathode. *J. Mater. Chem. A* **3**, 22846–22852 (2015).

34. Han, M. H. *et al*. High-Performance P2-Phase Na$_{2/3}$Mn$_{0.8}$Fe$_{0.1}$Ti$_{0.1}$O$_2$ Cathode Material for Ambient-Temperature Sodium-Ion Batteries. *Chem. Mater.* **28**, 106–116 (2016).

35. Komaba, S. *et al*. Study on the reversible electrode reaction of Na$_{1-x}$Ni$_{0.5}$Mn$_{0.5}$O$_2$ for a rechargeable sodium-ion battery. *Inorg. Chem.* **51**, 6211–6220 (2012).

36. Shanmugam, R. & Lai, W. Study of Transport Properties and Interfacial Kinetics of Na$_{2/3}$[Ni$_{1/3}$Mn$_x$Ti$_{2/3-x}$]O$_2$ ($x = 0, 1/3$) as Electrodes for Na-Ion Batteries. *J. Electrochem. Soc.* **162**, A8–A14 (2015).

37. Shanmugam, R. & Lai, W. Na$_{2/3}$Ni$_{1/3}$Ti$_{2/3}$O$_2$: ebi-functional f electrode materials for Na-ion batteries. *ECS Electrochem. Lett.* **3**, A23–A25 (2014).

38. Sharma, N. *et al*. Rate Dependent Performance Related to Crystal Structure Evolution of Na$_{0.67}$Mn$_{0.8}$Mg$_{0.2}$O$_2$ in a Sodium-Ion Battery. *Chem. Mater.* **27**, 6976–6986 (2015).

39. Wang, X., Tamaru, M., Okubo, M. & Yamada, A. Electrode Properties of P2-Na$_{2/3}$Mn$_y$Co$_{1-y}$O$_2$ as Cathode Materials for Sodium-Ion Batteries. *J. Phys. Chem. C* **117**, 15545–15551 (2013).

40. Wang, Y., Xiao, R., Hu, Y.-S., Avdeev, M. & Chen, L. P2-Na$_{0.6}$[Cr$_{0.6}$Ti$_{0.4}$]O$_2$ cation-disordered electrode for high-rate symmetric rechargeable sodium-ion batteries. *Nat. Commun.* **6**, 6954(9) (2015).

41. Yuan, D. *et al*. P2-type Na$_{0.67}$Mn$_{0.65}$Fe$_{0.2}$Ni$_{0.15}$O$_2$ Cathode Material with High-capacity for Sodium-ion Battery. *Electrochim. Acta* **116**, 300–305 (2014).

42. Zhao, J. *et al*. Electrochemical and thermal properties of P2-type Na$_{2/3}$Fe$_{1/3}$Mn$_{2/3}$O$_2$ for Na-ion batteries. *J. Power Sources* **264**, 235–239 (2014).

43. Zhao, W. *et al*. Synthesis of metal ion substituted P2-Na$_{2/3}$Ni$_{1/3}$Mn$_{2/3}$O$_2$ cathode material with enhanced performance for Na ion batteries. *Mater. Lett.* **135**, 131–134 (2014).

44. Zhao, W. *et al*. Enhanced electrochemical performance of Ti substituted P2-Na$_{2/3}$Ni$_{1/4}$Mn$_{3/4}$O$_2$ cathode material for sodium ion batteries. *Electrochim. Acta* **170**, 171–181 (2015).

45. Mortemard de Boisse, B., Carlier, D., Guignard, M., Bourgeois, L. & Delmas, C. P2-Na$_x$Mn$_{1/2}$Fe$_{1/2}$O$_2$ Phase Used as Positive Electrode in Na Batteries: Structural Charges Induced by the Electrochemical (De)intercalation Process. *Inorg. Chem.* **53**, 11197–11205 (2014).

46. Takada, K. *et al*. Superconductivity in two-dimensional CoO$_2$ layers. *Nature* **422**, 53–55 (2003).

47. Berthelot, R., Carlier, D. & Delmas, C. Electrochemical investigation of the P2-Na$_x$CoO$_2$ phase diagram. *Nat. Mater.* **10**, 74–80 (2011).

48. Huang, Q. *et al*. Coupling between electronic and structural degrees of freedom in the triangular lattice conductor Na$_x$CoO$_2$. *Phys. Rev. B* **70**, 184110 (2004).

49. Viciu, L. *et al*. Crystal structure and elementary properties of Na$_x$CoO$_2$ ($x = 0.32, 0.51, 0.6, 0.75$, and 0.92) in the three-layer NaCoO$_2$ family. *Phys. Rev. B* **73**(1), 74104(10) (2006).

50. Guignard, M. *et al*. Vanadium Clustering/Declustering in P2-Na$_{1/2}$VO$_2$ Layered Oxide. *Chem. Mater.* **26**, 1538–1548 (2014).

51. Kubota, K. *et al*. New insight into structural evolution in layered NaCrO$_2$ during electrochemical sodium extraction. *J. Phys. Chem. C* **119**, 166–175 (2015).

52. Jung, Y. H., Christiansen, A. S., Johnsen, R. E., Norby, P. & Kim, D. K. *In Situ* X-Ray Diffraction Studies on Structural Changes of a P2 Layered Material during Electrochemical Desodiation/Sodiation. *Adv. Funct. Mater.* **25**, 3227–3237 (2015).

53. Lu, X. *et al*. Direct imaging of layered O3- and P2-Na$_x$Fe$_{1/2}$Mn$_{1/2}$O$_2$ structures at the atomic scale. *Phys. Chem. Chem. Phys.* **16**, 21946–21952 (2014).

54. Shimono, T., Tanabe, D., Kobayashi, W. & Moritomo, Y. Structural Response of P2-Type Na$_x$MnO$_2$ against Na$^+$ Intercalation. *J. Phys. Soc. Jpn.* **82**, 083601 (2013).

55. Shimono, T., Tanabe, D., Kobayashi, W., Nitani, H. & Moritomo, Y. Electronic State of P2-Type Na$_x$MO$_2$ (M= Mn and Co) as Investigated by *In situ* X-ray Absorption Spectroscopy. *J. Phys. Soc. Jpn.* **82**, 124717(5) (2013).

56. Tanabe, D., Shimono, T., Kobayashi, W. & Moritomo, Y. Temperature dependence of anisotropic displacement parameters in O3-type NaMO$_2$ (M = Cr and Fe): Comparison with isostructural LiCoO$_2$. *Phys. Status Solidi - Rapid Res. Lett.* **8**, 287–290 (2014).

57. Tanabe, D., Shimono, T., Kobayashi, W. & Moritomo, Y. Na-site energy of P2-type Na_xMO_2 (M=Mn and Co). *Phys. Status Solidi RRL* **7**, 1097–1101 (2013).
58. Clarke, S. J., Fowkes, A. J., Harrison, A., Ibberson, R. M. & Rosseinsky, M. J. Synthesis, Structure, and Magnetic Properties of $NaTiO_2$. *Chem. Mater.* **10**, 372–384 (1998).
59. McQueen, T. M. *et al.* Successive orbital ordering transitions in $NaVO_2$. *Phys. Rev. Lett.* **101**, 166402 (2008).
60. McQueen, T. M. *et al.* Magnetic Structure and Properties of the $S = 5/2$ Triangular Antiferromagnet α-$NaFeO_2$. *Phys. Rev. B* **76**, 024420 (2007).
61. Onoda, M. Geometrically frustrated triangular lattice system Na_xVO_2: superparamagnetism in $x = 1$ and trimerization in $x \approx 0.7$. *J. Phys. Condens. Matter* **20**, 145205 (2008).
62. Lee, M. *et al.* Large enhancement of the thermopower in Na_xCoO_2 at high Na doping. *Nat. Mater.* **5**, 537 (2006).
63. Fujita, K., Mochida, T. & Nakamura, K. High-Temperature Thermoelectric Properties of $Na_xCoO_{2-\delta}$ Single Crystals. *Jpn. J. Appl. Phys.* **40**, 4644–4647 (2001).
64. Kim, S., Ma, X., Ong, S. P. & Ceder, G. A comparison of destabilization mechanisms of the layered Na_xMO_2 and Li_xMO_2 compounds upon alkali de-intercalation. *Phys. Chem. Chem. Phys.* **14**, 15571–15578 (2012).
65. Mo, Y., Ong, S. P. & Ceder, G. Insights into Diffusion Mechanisms in P2 Layered Oxide Materials by First-Principles Calculations. *Chem. Mater.* **26**, 5208–5214 (2014).
66. Toumar, A. J., Ong, S. P., Richards, W. D., Dacek, S. & Ceder, G. Vacancy Ordering in O3-Type Layered Metal Oxide Sodium-Ion Battery Cathodes. *Phys. Rev. Appl.* **4**, 064002(9) (2015).
67. Hinuma, Y., Meng, Y. S. & Ceder, G. Temperature-concentration phase diagram of P2-Na_xCoO_2 from first-principles calculations. *Phys. Rev. B* **77**, 224111 (2008).
68. Goodenough, J. B. & Kim, Y. Challenges for Rechargeable Li Batteries. *Chem. Mater.* **22**, 587–603 (2010).
69. Park, J.-K.(ed) Principles and Applications of Lithium Secondary Batteries. Wiley-VCH Verlag GmbH & Co. KGaA (2012).
70. Motohashi, T. *et al.* Impact of lithium composition on the thermoelectric properties of the layered cobalt oxide system Li_xCoO_2. *Phys. Rev. B* **83**, 195128 (2011).
71. Lan, R. & Tao, S. Novel Proton Conductors in the Layered Oxide Material $Li_xAl_{0.5}Co_{0.5}O_2$. *Adv. Energy Mater.* **4**, 1301683 (2014).
72. Sparks, T. D., Gurlo, A. & Clarke, D. R. Enhanced n-type thermopower in distortion-free $LiMn_2O_4$. *J. Mater. Chem.* **22**, 4631 (2012).
73. da Luz, M. S. *et al.* High-resolution measurements of the thermal expansion of superconducting Co-doped $BaFe_2As_2$. *Phys. Rev. B* **79**, 214505 (2009).
74. Shannon, R. D. Revised effective ionic radii and systematic studies of interatomic distances in halides and chalcogenides. *Acta. Cryst. A* **32**, 751 (1976).
75. Togo, A. & Tanaka, I. First principles phonon calculations in materials science. *Scripta Mater.* **108**, 1–5 (2015).
76. George, J. *et al.* Lattice thermal expansion and anisotropic displacements in α-sulfur from diffraction experiments and first-principles theory. *J. Chem. Phys.* **145**, 234512 (2016).
77. Souvatzis, P. & Eriksson, O. *Ab initio* calculations of the phonon spectra and the thermal expansion coefficients of the 4d metals. *Phys. Rev. B* **77**, 024110 (2008).
78. Palumbo, M. & Dal Corso, A. Lattice dynamics and thermophysical properties of h.c.p. Os and Ru from the quasi-harmonic approximation. *J. Phys.: Condens. Matter* **29**, 395401 (2017).
79. Erba, A., Shahrokhi, M., Moradian, R. & Dovesi, R. On how differently the quasi-harmonic approximation works for two isostructural crystals: Thermal properties of periclase and lime. *J. Chem. Phys.* **142**, 044114 (2015).
80. Wang, Z., Wang, F., Wang, L., Jia, Y. & Sun, Q. First-principles study of negative thermal expansion in zinc oxide. *J. Appl. Phys.* **114**, 063508 (2013).
81. Nishibori, E. *et al.* The large Debye-Scherrer camera installed at SPring-8 BL02B2 for charge density studies. *Nucl. Instrum. Methods A* **467-468**, 1045 (2001).
82. Izumi, F. & Momma, K. Three-Dimensional Visualization in Powder Diffraction. *Solid State Phenom.* **130**, 15 (2007).
83. Momma, K. & Izumi, F. *VESTA 3* for three-dimensional visualization of crystal, volumetric and morphology data. *J. Appl. Cryst.* **44**, 1272–1276 (2011).

Acknowledgements

Author Contributions

W.K. measured synchrotron XRD patterns, analyzed the XRD data, calculated linear thermal expansion coefficient based on a hard-sphere model, and wrote the manuscript. A.Y. synthesized O3-type layered oxides, and measured synchrotron XRD patterns. T.A., T.S., and D.T. synthesized P2-type layered oxides, and measured synchrotron XRD patterns. Y.M. contributed discussion and critically examined the manuscript.

Additional Information

Supplementary information accompanies this paper at https://doi.org/10.1038/s41598-018-22279-9.

Competing Interests: The authors declare no competing interests.

Publisher's note: Springer Nature remains neutral with regard to jurisdictional claims in published maps and institutional affiliations.